# Achieving beyond-100-GHz large-signal modulation bandwidth in hybrid silicon photonics Mach Zehnder modulators using thin film lithium niobate

Cite as: APL Photon. 4, 096101 (2019); doi: 10.1063/1.5115243 Submitted: 16 June 2019 • Accepted: 28 August 2019 •

Published Online: 13 September 2019







Xiaoxi Wang,¹ Peter O. Weigel,¹² Jie Zhao,¹ Michael Ruesing,¹ 📵 and Shayan Mookherjea¹

### **AFFILIATIONS**

- Department of Electrical and Computer Engineering, University of California, San Diego, La Jolla, California 92093-0407, USA
- <sup>2</sup>Jet Propulsion Laboratory, California Institute of Technology, 4800 Oak Grove Drive, Pasadena, California 91109, USA

Note: This article is part of the Special Topic on Hybrid Integration beyond Silicon Photonics.

# **ABSTRACT**

Mach-Zehnder electro-optic modulators (EOM) based on thin-film lithium niobate bonded to a silicon photonic waveguide circuit have been shown to achieve very high modulation bandwidths. Open eye-diagram measurements made in the time domain of beyond-small-signal modulation are used to support the modulation-sideband measurements in showing that such EOM's can support high-frequency modulations well beyond 100 GHz.

© 2019 Author(s). All article content, except where otherwise noted, is licensed under a Creative Commons Attribution (CC BY) license (http://creativecommons.org/licenses/by/4.0/). https://doi.org/10.1063/1.5115243

## I. INTRODUCTION

Optical communication, radio frequency photonic systems, and millimeter-wave test and measurement instrumentation which use optical devices nowadays require increasingly high bandwidths from integrated electro-optical modulators (EOM's), up to the subterahertz and terahertz bands in some cases. In semiconductor (silicon and III-V) photonic modulators, electronic carrier transit-time limitations fundamentally impact the very high frequency operation of diode-based EOM's, which has led to considerable interest in the study of alternative materials for EOM's. Modern III-V (e.g., InP) high-speed coherent modulators are being developed for 100 Gbaud, 400 Gbaud, and faster communication systems, but these devices can be challenging to realize, especially with high linearity, low chirp, and over the same broad range of wavelengths that dielectric electro-optic materials, such as lithium niobate, can cover. It is preferable that the fabrication approaches for such EOM's is compatible with the modern semiconductor fabrication methods nowadays used in silicon or III-V integrated photonics, which have generally led to improved functionality, cost reductions, and better manufacturing scalability compared to previous integrated optics technology.

This manuscript focuses on hybrid EOM's, in which a thin-film of electro-optically active material is used closely alongside other structures, features, and materials defined in the host semiconductor material, which serve many other functions that are desirable in a modern photonic integrated circuit (PIC). For example, integration of hybrid EOM's with other elements of the silicon PIC platform would benefit the development of higher-frequency active photonic microwave filters. A scalable fabrication approach to high-frequency Mach-Zehnder modulators (MZM's) could extend the range of frequency operation for the programmable RF processors studied recently. These are envisioned as very large scale PIC's, consisting of dozens to hundreds of individually addressed EOM's, and including other types of optical waveguide circuit elements, which would be difficult to fabricate using serial-write technology (e.g., electron-beam lithography) over large areas.

Ideally, CMOS-compatible processing and materials would be used for most of the fabrication process flow, with the nontraditional

material processing being performed at the back-end, respecting the process constraints (e.g., temperature, solvent compatibility, etc.) of the structures that have already been formed. Since a large number of component building blocks have already been developed in the silicon photonics ecosystem, it is useful to ask if ultrahigh frequency MZM's using lithium niobate (LN) can be developed in a way which is compatible with silicon photonics. Lithium niobate is an inorganic ferroelectric dielectric material that is widely used in field-deployed MZM's. 5,6 Over the past two decades, there have been several reports and studies of thin-film LN EOMs.<sup>7-23</sup> There is active effort underway to adapt the design and fabrication of LN MZM's to be compatible with modern integrated silicon photonics fabrication technology, including heterogeneous integration with silicon photonics components. Here, we should also mention that recent developments in hybrid MZM's using plasmonic effects and organic electro-optic material have shown subterahertz modulation bandwidth. 24,25 However, the principles of such modulators are quite different from the LN EOM's which are the focus of this paper.

In a recent publication, <sup>26</sup> we reported the fabrication and measurements of a hybrid silicon photonic modulator in which thinfilm LN was bonded over a part of the silicon (Si) photonic integrated optical circuit and was used to realize a high frequency MZM. The LN thin film was not etched, sawed, or otherwise processed after bonding, and all the waveguiding features were defined in the Si layer before bonding, using deep ultraviolet (DUV) photolithography. The EOM achieved beyond 105 GHz 3-dBe electrical bandwidth measured using the sideband technique (the sideband amplitude of the modulated optical signal is measured on an optical spectrum analyzer). The upper range of the measurement, being limited by available equipment, indicated only the 1.5 dBe electrical modulation bandwidth rather than the 3-dBe point. The modulated sideband technique can be used with small-signal modulation (a typical peak-to-peak voltage is 1 V), and therefore, a question remains whether, at these very high frequencies, the hybrid modulator can be used for modulation beyond the small-signal regime. In this manuscript, we report measurements where the driving

voltage is a significant fraction of the half-wave voltage,  $V_{\pi}$ , which result in open time-domain "eye diagrams" beyond 100 GHz RF modulation. These results are thus a significant addition to those presented earlier for the hybrid LN MZM. <sup>26</sup>

# II. THIN-FILM LN EOM INTEGRATION WITH SILICON PHOTONICS

Thin-film lithium niobate on insulator (LNOI),<sup>27</sup> consisting of a thin film of crystalline LN bonded to an oxide buffer layer and a handle (typically LN or silicon, Si), is now available from commercial sources and is an attractive material for initiating the heterogeneous integration process into a silicon photonics platform. However, as Fig. 1 shows, the size of available LNOI wafers is limited to about 3 or 4 in. in diameter, whereas the silicon on insulator (SOI) wafers used in a typical silicon photonics platform are 8 in. or 12 in. in diameter. Thus, building a PIC on an LNOI wafer is limited to small sizes, limited scalability, and must be fabricated outside typical silicon semiconductor foundries. Moreover, LN is not always convenient as a layer component for all types of photonic components. Thus, we have developed a die bonding approach, in which segmented dies from the LNOI wafer are bonded to the desired sites on the silicon PIC's which have been patterned on a foundry silicon photonic process on much larger wafers than currently possible in LNOI.2

In contrast with the earlier bonding studies between unpatterned LN and Si,  $^{29-31}$  the approach we and others have used is to perform bonding after the waveguiding features have been fabricated, i.e., one of the dies has Si or  $\rm Si_3N_4$  rib waveguides, over which  $\rm SiO_2$  is deposited, and planarization is performed using a chemical-mechanical polishing (CMP) process. We are able to bond over a large reticle-sized area (several square centimeters).  $^{26,28,32}$  (Hybrid LN-Si microring resonators can use a much smaller bonded area.  $^{33}$ ) In our approach, once the bonding of the LN film is complete, no further processing of the LN film is performed. In particular, there was no etching of LN which is performed in some approaches  $^{15,17,18,34,35}$  or sawing of the

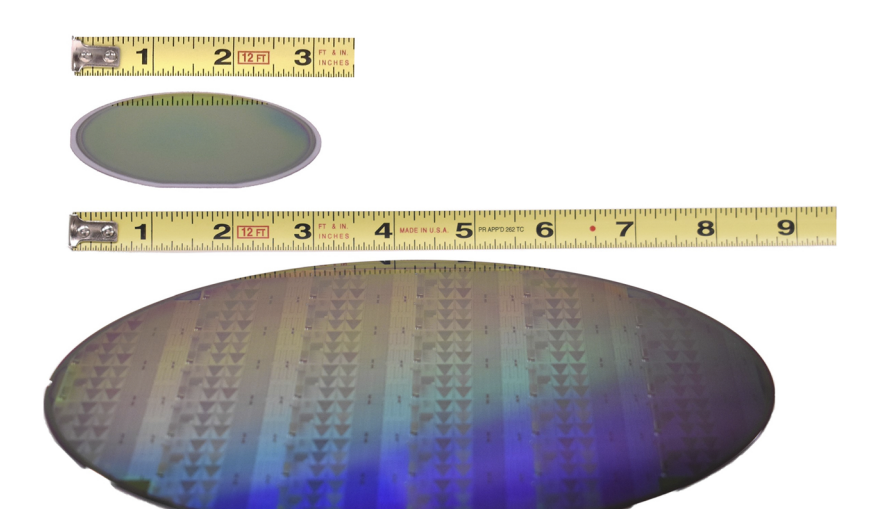


**FIG. 1.** Size comparison of thin-film lithium niobate on an insulator wafer (diameter 76 mm) and a silicon photonic wafer (diameter 200 mm), with patterned waveguide features, after chemical mechanical polishing (CMP).

 ${\rm LN,^{36}}$  or deposition and patterning of additional layers for optical waveguiding. <sup>37</sup>

It has been explained how the Si-LN hybrid waveguide supports small-radius bends, low loss transitions under the edge of the bonded LN film, and low-loss polarization-preserving mode transitions between an optical mode that is primarily localized in the Si region and one that is primarily localized in the LN film, with both materials being crystalline and of high quality.<sup>26,28</sup> Because of the hybrid mode design and interlayer transitions achieved using adiabatic waveguide tapers, the edges of the bonded thin film, even if rough on the scale of the optical wavelength, do not significantly affect optical propagation. This makes the back-end integration of thin-film LN simple and feasible, without requiring precision alignment or etching or patterning of either LN or silicon after bonding. The hybrid Si-LN TE-polarized waveguide mode used in the EOM reported in Ref. 26 achieved a (Poynting power) confinement fraction in the (unetched) LN layer calculated as  $\Gamma_{LN}=81\%$  and  $\Gamma_{Si}=5\%$ (the rest of the light is in the oxide). In view of the very small amount of light in Si, it may be argued that not much further improvement can be achieved by eliminating the Si altogether. Doing so would then require the LN slab to be etched, in order to provide some lateral confinement. Some studies have described benefits in performing both bonding and etching of thin-film LN, at the cost of significantly increased fabrication complexity and incompatibility with CMOS-compatible processing.

In our fabrication approach, depicted in Fig. 2, the hybrid x-cut LN Mach-Zehnder EOM's were built using commercially available LNOI wafers (NanoLN, Jinan Jingzheng Electronics Co., Ltd.) together with an established silicon photonics platform. We have based our fabrication on the multi-project wafer (MPW) silicon photonics process offered by Sandia National Laboratories. In our process, all features were defined using only photolithography, rather than electron-beam lithography, and did not require subresolution features, unlike, for example, plasmonic or polymeric slot modulators.  $^{39,40}$  The silicon photonic features were patterned on a high-resistivity Si handle wafer, with a measured resistivity (after HF etch to remove native oxide) of around  $6 \times 10^3 \Omega$ –cm.

In a traditional high-speed LN modulator with co-planar waveguide RF electrodes, the microwave index  $n_m$  is slightly greater than 4, which is much larger than the typical value of the optical

refractive index, which is around 2.2. The thicknesses of the oxide buffer layer under the electrodes, and of the electrodes themselves, are increased, which increases the capacitance of the RF transmission line, and thus, decreases the microwave index,  $n_m$ . Increasing the buffer thickness draws the RF field out of LN and into the buffer layer, which has a lower dielectric constant. Increasing the electrode thickness moves the RF field out of the buffer layer into air, thus increasing the effective area of the capacitor that is formed between the edges of the electrodes. Both of these effects, though helping to achieve index matching, result in a less efficient EOM. A traditional high-bandwidth LN MZI modulator can use gold electrode thicknesses of up to 19  $\mu$ m, and only a few reports of such EOM's have demonstrated a 3-dB electrical bandwidth in excess of 50 GHz. In the hybrid modulator, similar to the thin-film LN modulator without the bonded Si rib waveguide, 41 the situation is reversed: the microwave index is lower than the optical group index. With the inclusion of the Si rib waveguide, in particular, there is a relatively simple way of matching the indices. We defined the waveguiding features in the Si layer alone, with the only variations occuring in the width of the Si rib, and with no etching or patterning of the LN layer. In our test wafers, the Si layer thickness of 150 nm was achieved by thickness reduction from the original crystalline Si layer thickness of 230 nm in the starting SOI wafer, but could alternatively be achieved over specific sites by etching. Waveguide features were patterned by conventional Si processing, followed by oxide deposition and subsequent chemical mechanical polishing (CMP) and oxide thinning by a timed wet etch (diluted hydrofluoric acid) process. These are important steps in our hybrid integration process which is based on room-temperature oxide bonding (as contrasted, for example, with polymer adhesive bonding<sup>38</sup>).

Oxide,  $SiO_2$ , is the buffer material in both traditional LN and thin-film MZM's. Inclusion of thin  $SiO_2$  layers between the electrodes and LN have been studied in the past, with a view to improving the matching of the RF and optical refractive indices, which is crucial for achieving high bandwidth, and also to reduce optical propagation loss. However, increasing the thickness of this oxide layer results in lowering the modulation efficiency, and in general, results in a less efficient modulator. Here, there are (at least) two oxide layers, whose thicknesses can be varied (to different extents) in order to achieve index matching. The first is the relatively thin

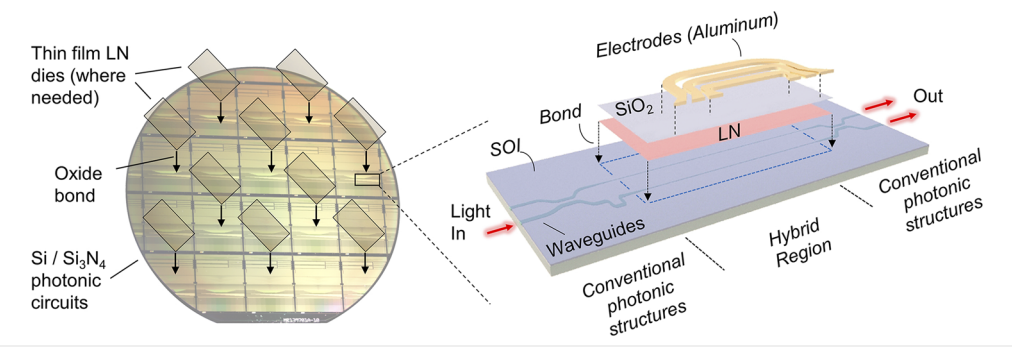


FIG. 2. Thin film x-cut lithium-niobate (LN) on insulator dies were bonded at room temperature to segmented dies of a patterned and planarized silicon-on-insulator (SOI) wafer which contained fabricated silicon or silicon nitride photonic waveguide circuits. No etching or patterning of the LN film was performed. To the right is shown an exploded representation of the EOM, where an unpatterned, unetched LN thin film was bonded to a Mach-Zehnder interferometer fabricated in Si

layer of oxide between the LN and the Si layers, which can be varied over a wide range, from a few tens of nanometers or less, to over a micron or more, during fabrication. We try to keep this oxide layer as thin as possible, in order to be able to transfer the optical power efficiently between the conventional silicon photonics mode outside the bonded region, and the hybrid mode. The second oxide layer thickness which matters is the total oxide thickness below the LN layer, up until the handle. An etched thin-film LN MZM which achieved 100 GHz modulation used a large buried oxide thickness of 4.7  $\mu$ m. In contrast, the standard photonics-grade silicon-oninsulator (SOI) wafers used in a foundry process have 2  $\mu$ m or 3  $\mu$ m oxide thickness. Since the RF losses in our coplanar electrode structure were low enough (as discussed below), we were able to retain compatibility with the foundry requirements, and used 3  $\mu$ m oxide thickness SOI wafers in our fabrication process.

The planarity and uniformity of the CMP process has improved in our recent work. In Fig. 3, we compare the measured oxide thickness above a patterned waveguide layer after thin oxide-layer CMP for our earlier results vs our recent developments (negative values correspond to regions where the oxide removal process was too aggressive and polished into the rib waveguide layer). Compared to our previous work, <sup>26</sup> the range of the variation of oxide thickness across the wafer has now been substantially reduced. A significant portion, but not all, <sup>26</sup> of the area of the earlier wafers was suitable for achieving 100 GHz modulation, with exclusions being seen along the periphery of the wafer. With the recent improvements in CMP, we expect to avoid nearly all exclusion zones across a typical 200 mm diameter wafer, alleviating a significant source of concern about the hybrid integration approach.

The rest of our MZM fabrication process is described in Ref. 26. We have shown that the bonded stack can withstand repeated temperature-cycling to at least 300 °C. This temperature budget is sufficient for the back-end fabrication process and many applications. Following bonding, the Si handle on the LNOI side was removed with an isotropic dry etch. The SiO<sub>2</sub> buffer layer supporting the LN thin film (as supplied in the starting wafer from the manufacturer) was removed with a wet etch; this step benefits from voidfree bonding, which in turn, relies upon good CMP. We used

deposited aluminum electrodes, rather than electroplated gold, to remain compatible with the materials and processing steps typically used in a CMOS-compatible Si photonics foundry-fabrication process. Aluminum was deposited by sputtering, after first sputtering a 10 nm chromium adhesion layer. Note that the electrodes are patterned directly on the LN layer (not on top of the handle), after the handle and the oxide (originally part of the LNOI wafer) was removed. A detailed discussion of the electrode design from an RF perspective is presented in Ref. 42. Several different types of coplanar waveguide (CPW) electrode structures were tested; typically, the electrode thickness was approximately 1.6 µm, the center (signal) electrode width was approximately 30  $\mu$ m, the outer (ground) electrodes had widths of about 100  $\mu$ m, and the electrode spacing was 12  $\mu$ m. All of these feature sizes are easy to achieve using photolithography. Note that the electrodes used here are more than 15 times thinner than those used in Ref. 43 and in traditional LN MZM's.4

In the search for the optimal electrode structure, we have reused the same bonded chips, repeatedly processing them (after bonding) through multiple cycles of electrode formation, removal, and reformation. In some cases, we refabricated electrodes several months after initial testing, after the contact pads were worn out through repeated probe landings during testing. Although dedicated reliability testing has not been performed, we did not observe debonding or noticeable degradation to the stability or quality of the samples during these additional process steps.

# **III. MEASUREMENTS**

We first summarize important aspects of the basic characterization of the hybrid MZM which support the direct high-frequency measurements presented below. From the measured transmission line S-parameters, the microwave refractive index,  $n_{\rm m}$ , and the characteristic impedance,  $Z_c$ , were calculated, using standard algebraic transformations and lossy transmission line circuit analysis. We infer  $n_{\rm m}=2.25$  and  $Z_c$  varied between 53.4 and 55.1  $\Omega$  from dc to 110 GHz. If both index and impedance were perfectly matched (neither is exactly true in our current designs), the RF-loss limited

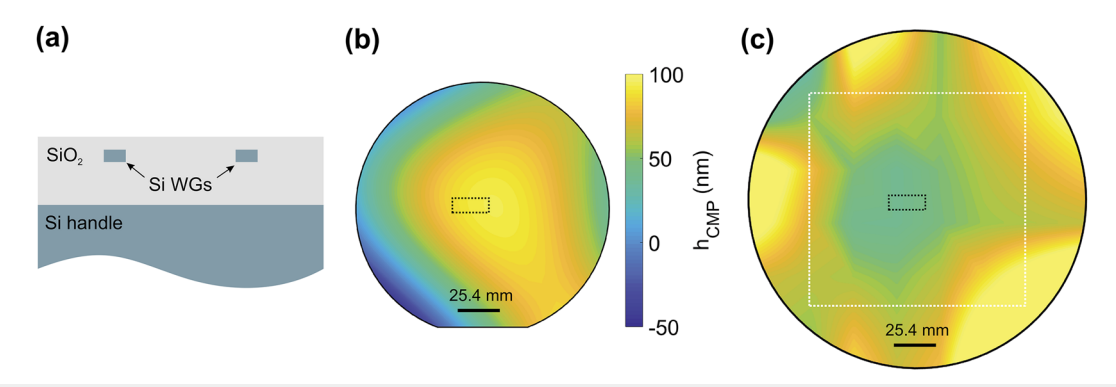


FIG. 3. (a) Cross section of the silicon photonic wafer, with rib features defined, after CMP. (b) Results of CMP, shown as a colormap of the height of the oxide layer above the patterned silicon rib features, after CMP, for our earlier attempts (150 mm diameter). (c) Recently improved results, on larger wafers (200 mm diameter), with silicon nitride rib features. The white dotted box shows the region in which ellipsometry data was measured; regions outside it are obtained by extrapolation during data processing. The black dotted box shows the size of a typical LN die which is bonded to fabricate the hybrid MZM.

bandwidth would result in a 3-dB point of  $\alpha_m(f_{3dB,el}).L=6.4$  dB. Our modulators which achieve greater than 100 GHz 3-dB electrical bandwidth have L=0.5 cm. If we require that the 3-dB electrical frequency  $f_{3dB,el} \geq 100$  GHz, then, we would need  $\alpha_m(100$  GHz)  $\leq 12.8$  dB cm $^{-1}$ . Measurements of the CPW showed  $\alpha_m(100$  GHz) =7.7 dB cm $^{-1}$ , which is well under the limit. Thus, even with a small deviation from perfect index and impedance matching, RF losses in our devices using thin aluminum electrodes are not a limitation to achieve higher than 100 GHz 3-dB electrical bandwidths.

In a MZM, low optical propagation loss does not impact the modulation bandwidth, but improves overall transmission. If the product of the optical waveguide loss coefficient times the phase shifter length is less than about 0.5 dB, the losses in a real device are usually dominated by nonidealities, such as imperfect chip coupling, or nonunitary power splitting at directional couplers, and further optical loss reduction plays only a minor role. There is some variability in the reported optical loss achieved when trying to process the thin lithium niobate layer. Whereas many etched thinfilm LN waveguides report optical propagation loss values of about 0.1-1 dB/cm, 20,46,47 lower optical propagation loss on the order of 0.01 dB/cm has been demonstrated in some etched thin-film LN waveguides 48,49 and in polished waveguides. 50 However, the etched thin-film LN MZM which supported 100 GHz modulation had 0.2 dB/cm loss.<sup>21</sup> In our hybrid Si-LN structures, the LN layer is not processed by etching or dicing. We have measured an optical propagation loss of 0.6 dB/cm in the hybrid Si-LN region, which has length of about 0.5 cm. As in common in practical modulators for packaging, we included 90° bends in the microwave transmission line to connect to the probe launch and termination pads, which had the same dimensions as the coplanar waveguide transmission line of the EOM. In contrast, some MZM's simply keep a straight layout for the CPW electrodes,<sup>21</sup> which may require additional steps for packaging, and can also lead to a different RF loss behavior (Sec. 5.4.2).

In a stand-alone, fiber-pigtailed EOM device using thin-film LN, another key loss parameter is the fiber-to-waveguide insertion loss and can be as low as 1.7 dB/facet. In a hybrid photonic integrated circuit, where there are other types of optical structures in the silicon layer which contribute to the overall functionality of the integrated circuit, an important parameter is the transition loss from silicon feeder waveguide into the hybrid mode, which was about 0.1 dB/transition in our device. Since the interlayer transition losses between silicon and silicon nitride layers can also be made low, we anticipate that hybrid LN integrated circuits can incorporate several back-and-forth passes through a bonded LN layer, for several different functionalities, well within the comparable loss budget of a traditional, single-function, stand-alone LN EOM device.

In previous work,<sup>26</sup> we reported the measured frequency response, where the method described in Ref. 53 was used to detect signals and modulation sidebands at an optical wavelength of 1560 nm; these data are shown here in Fig. 4(a) for comparison with the subsequent data. With the modulator biased at quadrature, the difference (log scale) between the optical intensity of the first sideband and carrier signal was used to extract the modulation index, and thus the frequency response, from 106 GHz down to 2 GHz (providing a safe margin for the 0.18 GHz resolution of the optical spectrum analyzer used in the measurement). We measured a flat-spectrum modulation response well past 105 GHz, as shown in Fig. 4(a), consistent with our simulation based on electrical S-parameter measurements, and the discussion presented in Secs. I and II of this paper, which predicts flat frequency response to even higher frequencies.

To show the time-domain modulation patterns, the drive voltage has to be a larger fraction of the half-wave voltage in order

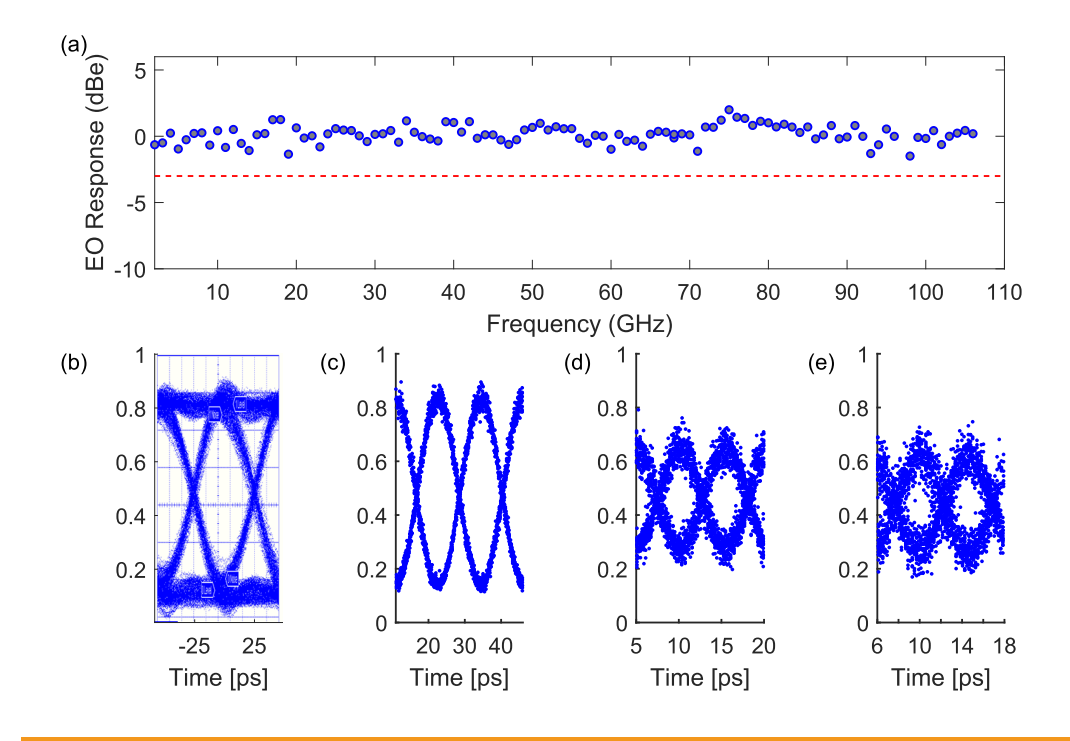


FIG. 4. (a) Electro-optic response of the hybrid LN MZM from sideband OSA measurements. Details of the measurement are reported in Ref. 26. (b) Eye diagram for 20 Gbit/s data modulation using a pseudorandom binary sequence. Modulation eye diagrams of large-signal RF sinusoidal modulation at increasingly high frequencies, (c) 40 GHz, (d) 90 GHz, and (e) 102 GHz. The vertical axis is in arbitrary units, proportional to optical power, with about 1000 points resolving the full scale. The offset of the horizontal time axis is arbitrary, with reference to a stable sampling clock at 80 MHz used in the sampling oscilloscope instrumentation.

to result in open "eye" diagrams. We show these eye diagrams captured using a sampling optical oscilloscope. In Fig. 4(b), we show a modest-speed eye diagram (20 Gbit/s) using on-off keying (OOK) modulation, generated using off-the-shelf optical communications test equipment, with an arbitrary waveform generator (AWG) generating a pseudorandom binary sequence (PRBS) digital data sequence. No probe, cable or detector compensation, or pre-emphasis was applied in this measurement. In Figs. 4(c)-4(e), we show the measured modulation patterns when driving the EOM with a sinusoidal waves of increasingly high frequency, extending beyond 100 GHz, which is well beyond the analog bandwidth of the arbitrary-waveform generators available today (Keysight M8194A, 45 GHz). At these extremely high frequencies, we used millimeterwave discrete components to generate an RF modulation tone. Thus, these ultra-high-frequency eye diagrams lack the 0-level and 1-level traces (i.e., the top and bottom parts of the eye), unlike the eye diagram in Fig. 4(b), but still reveal parametric information about the signal crossings, over- and undershoot, skew or asymmetry, and the opening. Although the eye opening gradually closes with increasing frequency, as expected, no skew, tilt, or vertical imbalance in the crossing point was evidenced.

The microwave signal was generated from a swept-frequency microwave CW oscillator (Anritsu). For generating RF frequencies up to 40 GHz, an RF amplifier (MITEQ) which was band limited to between 26 GHz and 40 GHz was used. For generation of RF frequencies greater than 40 GHz, a multiplier chain was used, which consisted of an RF synthesizer,  $6\times$  multiplier (AMC10, Millitech) which covers the frequency range 75 GHz–110 GHz (approximately), and GaAs and GaN amplifiers. The noise of these amplifiers is seen in the measured modulated waveforms, although the eye opening is still clearly visible at beyond 100 GHz. The output of the amplifier chain was coupled to a WR-10 waveguide, which was adapted to a 1.0 mm RF cable, incurring some loss in the signal power. The millimeter-wave signal was incident on the modulator microchip using 50  $\Omega$  ground-signal-ground (GSG) probes rated to 110 GHz. Calibration up to 110 GHz was performed using a

high-frequency RF power sensor and calibration substrates. We report measurements at the discrete modulation frequencies available in these experiments which were determined by the band-selective RF amplifiers.

Since the modulator microchip was not packaged and unoptimized fiber-waveguide couplers were used which incurred losses of up to 10 dB/facet, a specialized sampling oscilloscope apparatus<sup>54</sup> was used to detect the modulated waveform, which was then simply folded over in postprocessing, similar to a conventional optical sampling oscilloscope to create the eye diagram representation. The main reason for the use of the specialized oscilloscope<sup>54</sup> is its ability to accurately measure high-frequency modulation at low optical powers. This allows us to not use an optical amplifier to boost the power before photodetection, which is typical in conventional modulator measurements, and incurs noise.

The signal to noise ratio (Q) of the modulation pattern diagrams is calculated to be 12.5 dB at 40 GHz, 7.4 dB at 90 GHz, and 6.1 dB at 102 GHz. Although the eye diagram closes somewhat at 100 GHz in comparison to lower frequencies, the opening shown here is significantly greater than in 100 Gbit/s (70 GHz analog bandwidth,  $V_{\pi} = 7.4$  V) etched and bonded thin-film LN MZM's.<sup>38</sup>

The measured modulated waveforms were computationally processed to infer the EOM characteristics. First, a nonlinear least-squares fit to each of the modulated traces was performed using a raised-cosine function, 55 with an initial seed value for the fitting parameters (frequency and amplitude) obtained from a Fourier transform of the data. In Fig. 5(a), the vertical axis, labeled the extinction ratio, is defined as the ratio of the maximum to the minimum optical power of the modulation. Optical power was calculated by converting the number of counts to energy and dividing by the collection time. Differences in the output of the RF amplifiers at different frequencies were accounted by measuring the RF power before the probe pads.

Separately, the instrument response function (IRF), i.e., the impulse response of the detector apparatus, was measured and fitted to an exponentially modified Gaussian function whose

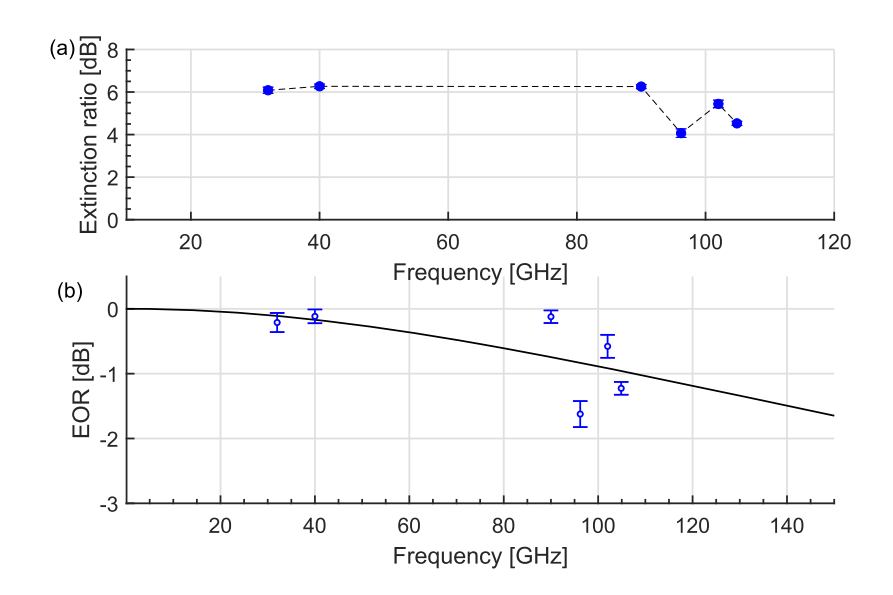


FIG. 5. (a) Extinction ratio vs modulation frequency for beyond small-signal analog modulation at discrete frequencies up to 105 GHz. Available frequencies were determined by the band limitations of the RF and millimeter-wave amplifiers. (b) The Electro-Optic Response (EOR), defined in the text, which characterizes the response of the hybrid modulator. The black line is a single-pole, low-pass filter fit to the data, which indicates a 3-dB cutoff frequency of 141 GHz.

full-width at half-maximum was  $t_{\text{FWHM}} = 6.3$  ps. The IRF is a jitterlike (zero-mean, finite-variance) noise contribution which results in spreading out the measured time-domain waveforms, i.e., an ideal delta-function-like sharp temporal response becomes spread laterally to neighboring time bins, and is reduced in amplitude at the peak time bin. Thus, the IRF results in reducing the amplitude measured in each temporal slice of the eye patterns shown in Fig. 4, compared to the "true" response of the device. We did not deconvolve the IRF in the modulation eye diagrams shown in Fig. 4, in order to show the raw measurements similar to the conventional oscilloscope (Agilent DCA-X), but in order to characterize the EOM response correctly, a correction factor is needed. The fitted amplitude of each sine wave was multiplied by a correction factor, whose value was calculated from the convolution between the fitted raised-cosine function and the measured IRF, with the latter being normalized to its probability density function. The correction factors were calculated to be  $(0.203)^{-1}$ ,  $(0.22)^{-1}$ ,  $(0.30)^{-1}$ ,  $(0.77)^{-1}$ , and (0.85)<sup>-1</sup> for RF frequencies of 105 GHz, 102 GHz, 90 GHz, 40 GHz, and 32 GHz, respectively.

The electro-optic response (EOR) is defined as EOR = OMA( $f_{RF}$ )/OMA(DC), where OMA( $f_{RF}$ ) is the Optical Modulation Amplitude at the RF frequency (e.g.,  $f_{RF} = 32, 40, ..., 105$ GHz), and OMA(DC) is its value at the DC voltage applied to the electro-optic modulator (the so-called biasing curve). The OMA is the defined in terms of the eye diagram (as usual) as the difference between the "1" and "0" power levels in Watts. Note that if the average power level varies between measurements (which is typical of using band-selective RF amplifiers to achieve large-signal modulation), the inferred OMA will be mathematically different even if the modulator achieves the same extinction ratio (ER, defined as the numerical ratio between the "1" and "0" power levels). Thus, we recorded the drive voltage at each frequency at which these measurements were performed and used it to renormalize the OMA. To be fair, we normalized all the measurements to the "worst-case" measurement which took the longest measurement time (unsurprisingly, at the highest modulation frequency limited by the available equipment, 104.88 GHz) for which the peak-to-peak voltage applied to the MZM electrodes was 4.45 V. (For comparison, the peakto-peak voltage for most of the range of the modulated-sideband measurement was between 0.7 V and 1 V.)

Once this renormalization is performed, ER then has a one-to-one mapping with the OMA so that the OMA used in the final EOR calculation is correctly referenced to a constant average power, and the frequency roll-off can be only then be correctly extrapolated. We fitted a single-pole low-pass response to the data, as shown in Fig. 5(b), which indicated in a 3-dB (electrical) roll-off at  $f_{3dB(E)}$  = 141 GHz. This is qualitatively consistent with the RF modulated-sideband measurements reported earlier, which indicated a 3-dB roll-off at frequencies well beyond 105 GHz.

# **IV. CONCLUSION**

The hybrid thin-film lithium niobate Mach-Zehnder electrooptic modulator can achieve >100 GHz 3-dB electrical bandwidths and is compatible with silicon photonics, both in the design and the fabrication process flow. In this hybrid MZM structure, the input and output are in silicon photonics and, through the use of interlayer vertical waveguide transitions, the device is not sensitive to the

rough edges, if any, of the LN thin film bonded to a section of the silicon PIC. Like the traditional EOM, this modulator utilizes the well-known Pockels electro-optic effect in LN which is a reliable and robust material; however, it only does so in the desired section of the light pathway and returns the optical mode to the silicon waveguide layer for other PIC functionality on the same microchip. Moreover, compared to the latter, the fabrication process for the hybrid MZM does not require etching or sawing of LN and is based on a standard silicon photonics foundry fabrication flow with a bonding step and relatively thin aluminum electrode formation at the back-end. The modulated sideband measurements reported earlier are augmented here with time-domain measurements of modulated waveforms, and analysis further supports the hypothesis that the hybrid modulator is a relatively simple, silicon-photonics-compliant structure which may be useful for applications involving electro-optic modulation well beyond 100 GHz.

# **ACKNOWLEDGMENTS**

The authors acknowledge funding support from the National Science Foundation (NSF) (Grant Nos. ECCS 1201308 and EFMA-1640968) and NASA (Grant Nos. NNX16AD14G and 80NSSC17K0166). Part of the research, including the W-band modulation, was performed at the Jet Propulsion Laboratory (JPL), California Institute of Technology, under contract with the National Aeronautics and Space Administration. The authors are grateful to B. A. Korzh, M. D. Shaw, D. J. Nemchick, and B. J. Drouin (NASA JPL), K. K. Berggren (MIT), and W. Becker (Becker and Hickl, GmbH) for assistance.

### **REFERENCES**

- <sup>1</sup>S. Jia, X. Pang, O. Ozolins, X. Yu, H. Hu, J. Yu, P. Guan, F. D. Ros, S. Popov, G. Jacobsen, M. Galili, T. Morioka, D. Zibar, and L. K. Oxenlowe, J. Lightwave Technol. **36**, 610 (2018).
- <sup>2</sup>J. S. Fandiño, P. Muñoz, D. Doménech, and J. Capmany, Nat. Photonics 11, 124 (2016).
- <sup>3</sup>L. Zhuang, C. G. H. Roeloffzen, M. Hoekman, K.-J. Boller, and A. J. Lowery, Optica 2, 854 (2015).
- <sup>4</sup>D. Pérez, I. Gasulla, L. Crudgington, D. J. Thomson, A. Z. Khokhar, K. Li, W. Cao, G. Z. Mashanovich, and J. Capmany, Nat. Commun. **8**, 636 (2017).
- <sup>5</sup>M. Lawrence, Rep. Prog. Phys. **56**, 363 (1993).
- <sup>6</sup>E. L. Wooten, K. M. Kissa, A. Yi-Yan, E. J. Murphy, D. A. Lafaw, P. F. Hallemeier, D. Maack, D. V. Attanasio, D. J. Fritz, G. J. McBrien, and D. E. Bossi, IEEE J. Sel. Top. Quantum Electron. **6**, 69 (2000).
- <sup>7</sup>P. Rabiei and P. Gunter, Appl. Phys. Lett. **85**, 4603 (2004).
- <sup>8</sup>W. Sohler, H. Hu, R. Ricken, V. Quiring, C. Vannahme, H. Herrmann, D. Büchter, S. Reza, W. Grundkötter, S. Orlov *et al.*, Opt. Photonics News **19**, 24 (2008).
- <sup>9</sup>V. Stenger, J. Toney, A. Pollick, J. Busch, J. Scholl, P. Pontius, and S. Sriram, in Conference on Lasers and Electro-Optics (CLEO), 2013.
- <sup>10</sup>L. Cao, A. Aboketaf, Z. Wang, and S. Preble, Opt. Commun. 330, 40 (2014).
- <sup>11</sup>L. Chen, Q. Xu, M. G. Wood, and R. M. Reano, Optica 1, 112 (2014).
- <sup>12</sup>L. Chen, J. Chen, J. Nagy, and R. M. Reano, Opt. Express 23, 13255 (2015).
- <sup>13</sup> A. Rao, A. Patil, J. Chiles, M. Malinowski, S. Novak, K. Richardson, P. Rabiei, and S. Fathpour, Opt. Express 23, 22746 (2015).
- <sup>14</sup>S. Jin, L. Xu, H. Zhang, and Y. Li, IEEE Photonics Technol. Lett. 28, 736 (2016).
- <sup>15</sup> A. J. Mercante, P. Yao, S. Shi, G. Schneider, J. Murakowski, and D. W. Prather, Opt. Express 24, 15590 (2016).
- <sup>16</sup> A. Rao, M. Malinowski, A. Honardoost, J. R. Talukder, P. Rabiei, P. Delfyett, and S. Fathpour, Opt. Express 24, 29941 (2016).

- <sup>17</sup>V. E. Stenger, J. Toney, A. PoNick, D. Brown, B. Griffin, R. Nelson, and S. Sriram, in European Conference on Optical Communications, 2017.
- <sup>18</sup>C. Wang, M. Zhang, B. Stern, M. Lipson, and M. Lončar, Opt. Express 26, 1547 (2018).
- <sup>19</sup> A. J. Mercante, S. Shi, P. Yao, L. Xie, R. M. Weikle, and D. W. Prather, Opt. Express 26, 14810 (2018).
- <sup>20</sup> A. Boes, B. Corcoran, L. Chang, J. Bowers, and A. Mitchell, Laser Photonics Rev. 12, 1700256 (2018).
- <sup>21</sup> C. Wang, M. Zhang, X. Chen, M. Bertrand, A. Shams-Ansari, S. Chandrasekhar, P. Winzer, and M. Lončar, Nature 562, 101 (2018).
- <sup>22</sup>N. Boynton, M. Gehl, S. Arterburn, C. Dallo, A. Pomerene, A. Starbuck, D. Hood, D. Trotter, T. Friedmann, A. Lentine, and C. T. DeRose, in Proceedings Optical Interconnects Conference, 2019.
- <sup>23</sup> A. Honardoost, F. A. Juneghani, R. Safian, and S. Fathpour, Opt. Express 27, 6495 (2019).
- <sup>24</sup>C. Haffner, D. Chelladurai, Y. Fedoryshyn, A. Josten, B. Baeuerle, W. Heni, T. Watanabe, T. Cui, B. Cheng, S. Saha, D. L. Elder, L. R. Dalton, A. Boltasseva, V. M. Shalaev, N. Kinsey, and J. Leuthold, Nature 556, 483 (2018).
- <sup>25</sup> M. Burla, C. Hoessbacher, W. Heni, C. Haffner, Y. Fedoryshyn, D. Werner, T. Watanabe, H. Massler, D. L. Elder, L. R. Dalton, and J. Leuthold, APL Photonics 4, 056106 (2019).
- <sup>26</sup>P. O. Weigel, J. Zhao, K. Fang, H. Al-Rubaye, D. Trotter, D. Hood, J. Mudrick, C. Dallo, A. T. Pomerene, A. L. Starbuck, C. T. DeRose, A. L. Lentine, G. Rebeiz, and S. Mookherjea, Opt. Express 26, 23728 (2018).
- <sup>27</sup>G. Poberaj, H. Hu, W. Sohler, and P. Günter, Laser Photonics Rev. 6, 488 (2012).
- <sup>28</sup>P. O. Weigel, M. Savanier, C. T. DeRose, A. T. Pomerene, A. L. Starbuck, A. L. Lentine, V. Stenger, and S. Mookherjea, Sci. Rep. **6**, 22301 (2016).
- <sup>29</sup> H. Takagi, R. Maeda, N. Hosoda, and T. Suga, Appl. Phys. Lett. **74**, 2387 (1999).
- M. M. R. Howlader, T. Suga, and M. J. Kim, Appl. Phys. Lett. 89, 031914 (2006).
  R. Takigawa, E. Higurashi, T. Suga, S. Shinada, and T. Kawanishi, Proc. SPIE 6376, 637603 (2006).
- <sup>32</sup>P. Weigel and S. Mookherjea, Opt. Mater. **66**, 605 (2017).
- 33 Y. S. Lee, G.-D Kim, W.-J. Kim, S.-S. Lee, W.-G. Lee, and W. H. Steier, Opt. Lett. 36. 1119 (2011).
- <sup>34</sup>G. Ulliac, V. Calero, A. Ndao, F. I. Baida, and M.-P. Bernal, Opt. Mater. 53, 1 (2016).
- <sup>35</sup> M. Zhang, C. Wang, X. Chen, M. Bertrand, A. Shams-Ansari, S. Chandrasekhar, P. Winzer, and M. Lončar, in *Optical Fiber Communications Conference and Exposition (OFC)* (IEEE, 2018), pp. 1–3.

- <sup>36</sup>N. Courjal, F. Devaux, A. Gerthoffer, C. Guyot, F. Henrot, A. Ndao, and M.-P. Bernal, Opt. Express 23, 13983 (2015).
- <sup>37</sup>P. Rabiei, J. Ma, S. Khan, J. Chiles, and S. Fathpour, Opt. Express 21, 25573 (2013).
- <sup>38</sup> M. He, M. Xu, Y. Ren, J. Jian, Z. Ruan, Y. Xu, S. Gao, S. Sun, X. Wen, L. Zhou, L. Liu, C. Guo, H. Chen, S. Yu, L. Liu, and X. Cai, Nat. Photonics 13, 359 (2019).
- <sup>39</sup>S. Zhu, G. Q. Lo, and D. L. Kwong, Opt. Express 21, 8320 (2013).
- <sup>40</sup> M. Ayata, Y. Fedoryshyn, W. Heni, B. Baeuerle, A. Josten, M. Zahner, U. Koch, Y. Salamin, C. Hoessbacher, C. Haffner, D. L. Elder, L. R. Dalton, and J. Leuthold, Science 358, 630 (2017).
- <sup>41</sup>L. Gheorma, P. Savi, and R. M. Osgood, IEEE Photonics Technol. Lett. **12**, 1618 (2000).
- <sup>42</sup>P. O. Weigel, "High-speed hybrid silicon-lithium niobate electro-optic modulators and related technologies," Ph.D. thesis, UC San Diego, 2018.
- <sup>43</sup> K. Noguchi, O. Mitomi, and H. Miyazawa, J. Lightwave Technol. **16**, 615 (1998).
- <sup>44</sup>M. M. Howerton and W. K. Burns, "Broadband traveling wave modulators in LiNbO<sub>3</sub>," in *RF Photonic Technology in Optical Fiber Links* (Cambridge University Press, 2002), pp. 133–164.
- <sup>45</sup>D. M. Pozar, *Microwave Engineering*, 4th ed. (Wiley, 2012).
- <sup>46</sup>S. Y. Siew, E. J. H. Cheung, H. Liang, A. Bettiol, N. Toyoda, B. Alshehri, E. Dogheche, and A. J. Danner, Opt. Express 26, 4421 (2018).
- <sup>47</sup>I. Krasnokutska, J.-L. J. Tambasco, X. Li, and A. Peruzzo, Opt. Express 26, 897 (2018).
- (2018).  $^{48}$  M. Zhang, C. Wang, R. Cheng, A. Shams-Ansari, and M. Lončar, Optica 4, 1536 (2017).
- <sup>49</sup>B. Desiatov, A. Shams-Ansari, M. Zhang, C. Wang, and M. Lončar, Optica **6**, 380 (2019).
- <sup>50</sup> R. Wu, M. Wang, J. Xu, J. Qi, W. Chu, Z. Fang, J. Zhang, J. Zhou, L. Qiao, Z. Chai, J. Lin, and Y. Cheng, Nanomaterials 8, 910 (2018).
- <sup>51</sup> L. He, M. Zhang, A. Shams-Ansari, R. Zhu, C. Wang, and L. Marko, Opt. Lett. 44, 2314 (2019).
- <sup>52</sup>W. D. Sacher, J. C. Mikkelsen, P. Dumais, J. Jiang, D. Goodwill, X. Luo, Y. Huang, Y. Yang, A. Bois, P. G.-Q. Lo, E. Bernier, and J. K. S. Poon, Opt. Express 25, 30862 (2017).
- <sup>53</sup>Y. Shi, L. Yan, and A. E. Willner, J. Lightwave Technol. **21**, 2358 (2003).
- <sup>54</sup>X. Wang, B. A. Korzh, P. O. Weigel, D. J. Nemchick, B. J. Drouin, A. Fung, W. Becker, Q.-Y. Zhao, D. Zhu, M. Colangelo, A. E. Dane, K. K. Berggren, M. D. Shaw, and S. Mookherjea, in *Optical Fiber Communication Conference Postdeadline Papers* 2019, Th4C.1 (OSA, 2019).
- $^{55}$ G. Ghione, Semiconductor Devices for High-Speed Optoelectronics (Cambridge University, 2009).